IOP Publishing Phys. Scr. **100** (2025) 095016 https://doi.org/10.1088/1402-4896/ae03f0

Physica Scripta

OPEN ACCESS

RECEIVED
18 May 2025

REVISED
12 August 2025

ACCEPTED FOR PUBLICATION
5 September 2025

PUBLISHED
22 September 2025

Original content from this work may be used under the terms of the Creative Commons Attribution 4.0 licence.

Any further distribution of this work must maintain attribution to the author(s) and the title of the work, journal citation and DOI.

PAPER

Parametric amplification in a Josephson junction array Fabry-Pérot cavity

Javier Navarro Montilla[1,*], **Nikita Klimovich**[1], **Arnaud Barbier**[2], **Eduard F C Driessen**[2] and **Boon-Kok Tan**[1]

[1] Department of Physics (Astrophysics), University of Oxford, Denys Wilkinson Building, Keble Road OX1 3RH, Oxford, United Kingdom
[2] Institut de Radioastronomie Millimétrique (IRAM), Saint Martin d'Hères, 38406, France
[*] Author to whom any correspondence should be addressed.

E-mail: javier.navarro-montilla@stfc.ac.uk

Keywords: parametric amplification, Josephson arrays, Fabry-Pérot resonator, Superconducting device, Phase-sensitive amplification

Supplementary material for this article is available online

Abstract

Superconducting Parametric Amplifiers (SPAs) with near-quantum-limited added noise are crucial for weak signal detection applications such as astronomical receivers, quantum computation, and fundamental physics experiments. Commercially available SPAs include Josephson Parametric Amplifiers (JPAs), which offer high gain but narrow bandwidth performance; and Josephson-junction Travelling Wave Parametric Amplifiers (JTWPAs), which provide broader bandwidth at the cost of a complicated fabrication procedure, lower fabrication yield, and larger footprint area. In this paper, we investigate the parametric amplification of microwave signals in a Josephson array embedded in a low-Q Fabry-Pérot cavity. We fabricated a 500-junction array device and measured $>$15 dB phase-preserving gain over a $\sim$350 MHz bandwidth, while offering almost two orders of magnitude improvement in compression point ($P_{1\mathrm{dB}} = -106.2$ dBm) compared to standard JPAs. Furthermore, using a novel measurement technique, we configured our device to operate in the phase-sensitive mode, measuring a phase-sensitive extinction ratio (PSER) of 42.3 $\pm$ 2.81 dB, in line with state-of-the-art values for JPAs. These promising performances, combined with the ease of fabrication and improved yield compared with JTWPAs, underscore the potential of these devices for applications in advanced detection schemes.

1. Introduction

Microwave low-noise amplifiers (LNAs) are essential components for the readout of extremely weak signals. Their applications span from astrophysics, reading the output signal of receivers such as Superconductor-Insulator-Superconductor (SIS) mixers and Microwave Kinetic Inductance Detectors (MKIDs) [1, 2], to superconducting quantum computation platforms, permitting the dispersive readout of superconducting qubits [3]. Other applications include axion-like dark-matter particle search [4, 5] and fundamental physics experiments such as the detection of spontaneous down-conversion in Josephson junctions [6] and resonance spin electron experiments [7]. Phase-preserving amplifiers, where both the quadratures of the input signal are amplified, inherently add some noise in the amplification process as limited by the Heisenberg uncertainty principle [8]. In the microwave regime, Superconducting Parametric Amplifiers (SPAs) are the leading technology for quantum-limited amplification. SPAs utilise low-loss, nonlinear inductive elements as the medium for wave mixing and amplification. These elements include the current-dependent inductance of Josephson junctions (JJs), the flux-dependent inductance of superconducting quantum interference devices (SQUIDs), and the high kinetic inductance of disordered superconducting films. When a high-amplitude pump at frequency ω_p and a low-amplitude signal at frequency ω_s are injected into an SPA, the pump tone modulates the system's inductance, enabling energy transfer from the pump to the signal tone and thereby

© 2025 The Author(s). Published by IOP Publishing Ltd

amplifying the signal. In this process, an idler tone ω_{i} is generated for energy and momentum conservation, i.e., $2k_{\mathrm{p}} = k_{\mathrm{s}} + k_{\mathrm{i}}$ ($k_{\mathrm{p}} = k_{\mathrm{s}} + k_{\mathrm{i}}$) for a four(three)-wave mixing process, where k_{n} is the wavector associated to the ω_{n} tone, and $n = \{\mathrm{p}, \mathrm{s}, \mathrm{i}\}$.

The past two decades have seen a rapid development of SPAs, particularly with the implementation of the lumped-element Josephson Parametric Amplifier (JPA) [9]. Traditional JPAs embed a single (or a few) Josephson junction(s) in an LC resonator/cavity to enhance the interaction time between the pump and the signal. This results in high narrow-band gain around the resonance frequency. Despite their high gain ($\sim$15 to 30dB), simple fabrication and design, the bandwidth and compression point of JPAs are often limited to $\sim$100 MHz and ~ -120 dBm respectively, complicating certain applications such as simultaneous multi-qubit readout. To circumvent these limitations, Josephson Travelling Wave Parametric Amplifiers (JTWPAs) were developed [3]. JTWPAs use an array of thousands of Josephson junctions embedded in a long transmission line to provide the required mixing time and length for amplification while the electromagnetic tones propagate through the device. By removing the resonant architecture of JPAs, JTWPAs achieve high gain ($>$ 20 dB) over a much larger bandwidth, in the order of a few GHz. However, achieving this performance requires exceptional uniformity in the Josephson junction parameters, as variations can degrade gain and noise performance [10–12]. Moreover, the large number of components makes JTWPAs more susceptible to fabrication defects such as open-circuited junctions and pinholes [13, 14]. In addition, JTWPAs face intrinsic challenges such as pump depletion, which can further constrain their operational gain and dynamic range [15].

Ultimately, an ideal quantum-limited amplifier would have a high compression point, as well as high gain over a large bandwidth, while maintaining ease in the fabrication. To that end, impedance-matching techniques have been recently explored to increase the bandwidth of JPAs [16, 17]. Furthermore, several studies suggested using JJ arrays instead of single junctions in JPAs to improve their compression point [18, 19]. In this paper, we follow this latter approach to develop a device that could bridge the gain-bandwidth gap between resonant JPAs and JTWPAs. Our device consists of an array of JJs embedded in a low quality factor (Q) cavity, hereafter referred to as a Standing Wave Parametric Amplifier (SWPA). The moderate number of junctions required for the SWPA facilitates its fabrication yield compared to JTWPAs, while demonstrating an improved bandwidth and compression point against conventional JPA implementations [9, 20, 21]. We report the observation of four-wave mixing (4WM) phase-preserving gain ($>$15dB) when pumped around different orders of cavity modes with an enhanced bandwidth, up to $\sim$350 MHz, and a compression of ~ -100 dBm. Furthermore, we report on the observation of phase-sensitive amplification in this device using a novel measurement technique, demonstrating the potential of SWPAs to generate squeezed microwave states [22].

2. Device topology

These SWPA devices were fabricated as part of our effort to develop a broadband JTWPA. Before embarking in fabricating a JTWPA that requires thousands of Josephson junctions coupled with phase-matching and impedance-matching elements, we commence our programme with these relatively simple devices to better understand the fabrication yield of Josephson arrays. In the SWPA presented in this paper, we embedded 500 niobium (Nb) Josephson junctions along the central strip of a 50 Ω superconducting niobium coplanar waveguide (CPW) transmission line, depicted in figure 1. A microscope image of the device is shown in figure 2(a), with a cross-section schematic view of the different layers in figure 2(b). The junctions were fabricated using a standard niobium trilayer technique (details in the Supplementary Material).

The inclusion of the junction array modifies the characteristic impedance Z_0 of this section, moving it away from the nominal 50 Ω value, thus creating a Fabry-Pérot or etalon cavity. Consequently, the signal, pump, and idler tones reflect partially at the two ends of the cavity, with a reflection coefficient $\Gamma = \frac{Z_{\mathrm{jj}} - Z_0}{Z_{\mathrm{jj}} + Z_0}$, where Z_{jj} is the characteristic impedance of the junction array. These reflections cause the tones to bounce within the cavity, increasing their interaction time with the nonlinear junction array before exiting with parametric wave-mixing gain. Although conventional JPAs use capacitive-coupled cavities that achieve quality factors $Q = \frac{\omega_0}{\Delta\omega} \approx 50 - 500$ [19]—where $\Delta\omega$ is the bandwidth and ω_0 the resonance frequency—the cavity formed in our device as a result of the impedance mismatch results in a substantially lower $Q \sim 6$[3].

To compensate for the reduced parametric gain of a low-Q cavity, we packed a larger number of junctions with small spacing, which increases the inductance per unit length of the cavity and recovers the high gain performance. This approach suggests that further reducing the Q-value to broaden the operational bandwidth could be counterbalanced by adding even more junctions to maintain gain. However, since the operational

---

[3] The quality factor is estimated from the third resonant mode of the array in the transmission profile plotted in figure 3(c). We obtain: $Q = \frac{\omega_0}{\Delta\omega} \approx 9.3\,\mathrm{GHz}/1.56\ \mathrm{GHz} \approx 6$.

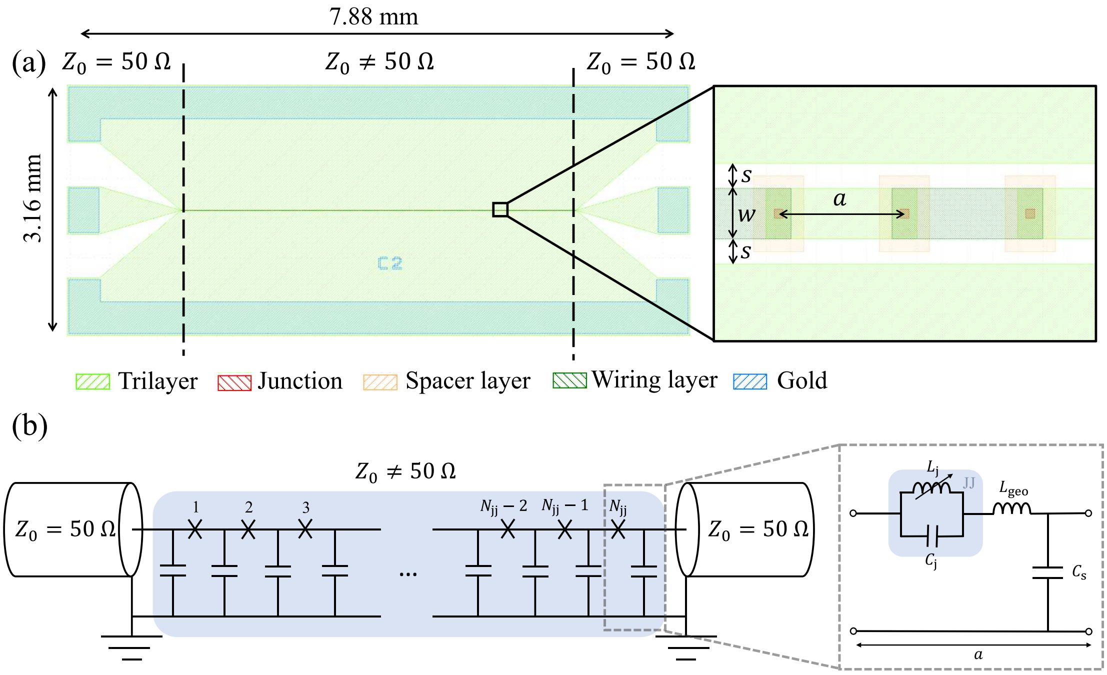

Figure 1. (a) SWPA chip layout showing the CPW transmission line with CPW gap $s = 2\ \mu$m, trace width $w = 4\ \mu$m, and junction separation $a = 10\ \mu$m. (b) Circuit diagram of the SWPA. A $Z_0 \neq 50\ \Omega$ line is formed by embedding a large number of junctions ($N_{jj} = 500$) along the CPW transmission line, creating a Fabry-Pérot cavity. The zoom-in sketch shows the unit cell of the SWPA.

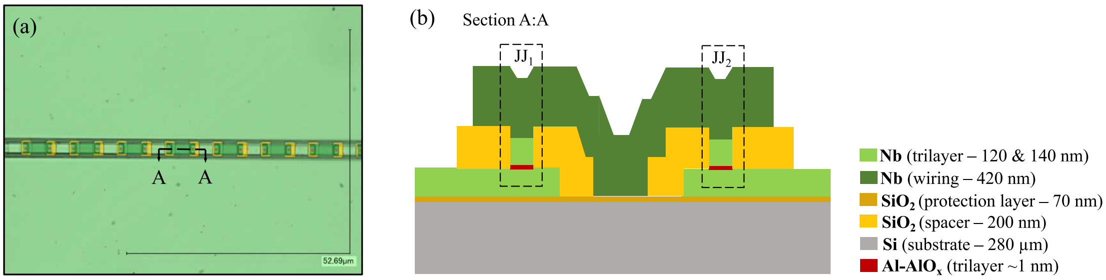

Figure 2. (a) Microscope image of a SWPA with fake colours representing the trilayer (light green), junctions (red), spacer layer (yellow), and wiring layer (dark green). (b) Illustration of the cross-section cut in A–A shown in (a).

central frequency of the SWPA is determined by the cavity length and there is a practical limit to how closely the junctions can be packed, this idea naturally leads to an ultra-low-Q cavity with sufficient nonlinear inductance per unit length, effectively creating a Josephson Travelling Wave Parametric Amplifier (JTWPA). Thus, our SWPA can be seen as a middle ground between traditional JPAs and JTWPAs. Unlike conventional JPAs, the SWPAs are two-port devices, allowing pump injection from either side of the device. Another advantage is their higher fabrication yield compared with JTWPAs, requiring approximately 75% fewer junctions.

Since the SWPA relies on the impedance mismatch between the junction-embedded section ($Z_0 \neq 50\ \Omega$) and the surrounding 50 Ω-impedance environment, no additional shunt capacitance structures (such as parallel-plate capacitors or interdigitated capacitors) are required to achieve 50 Ω like the case of JTWPAs. These components often suffer from fabrication defects, such as pin-hole formation in the dielectric layer [14]. Additionally, no phase-matching components, such as large-footprint resonators or periodic loading structures, are necessary. This simplifies the design, resulting in a straightforward topology that eases fabrication and improves yield. Moreover, the presence of many junctions relaxes the required magnitude of nonlinearity for each individual junction, allowing us to design them without the need for the low critical current values ($I_c < 4\mu$A), often used in JTWPA implementations. This naturally improves the compression point of our SWPAs compared to traditional JPAs [9, 20, 21].

Similar device topologies have been previously investigated using high-kinetic-inductance materials [23], or employing high-Q cavities formed by Superconducting Quantum Interference Devices (SQUIDs) [24] instead of bare Josephson junctions as in our case. Bare Josephson junction devices offer the advantage of

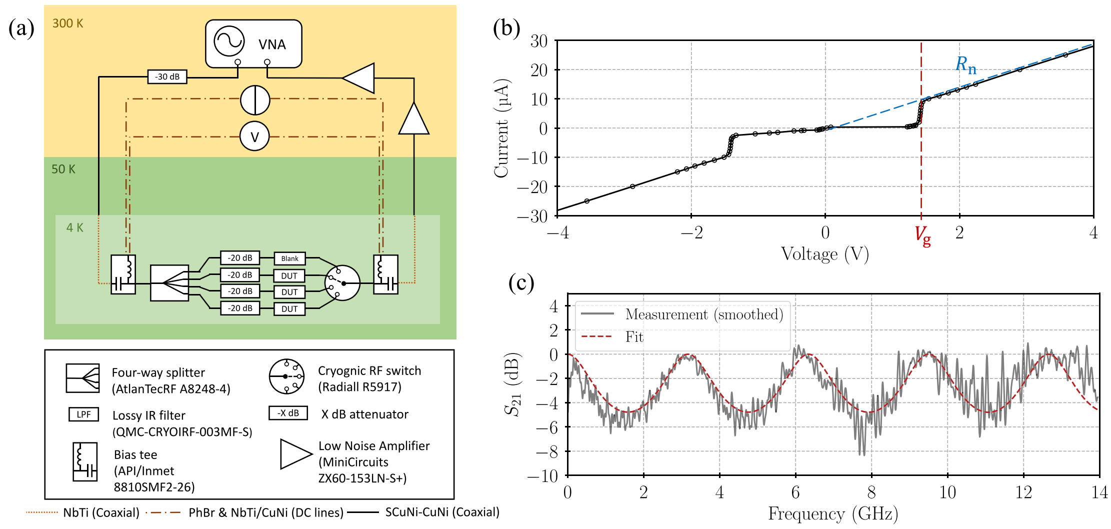

Figure 3. (a) Experimental Setup-A. We used a Keithley 6221 current source and Keithley 2182A voltmeter. (b) The measured IV curve of the SWPA from a downward current sweep, where $V_{\mathrm{gap}} = 1.42$ V. We extract the R_{n} value with a linear fit of the points above V_{g}, yielding $R_{\mathrm{n}} = 134.6$ kΩ. (c) The SWPA S_{21} transmission profile calibrated with respect to the 'blank'. The measured data was smoothed with a 50.4 MHz moving average window. The S_{21} sinusoidal variation with frequency originates from the Fabry-Pérot cavity, where the frequency of the resonant modes $f_{\mathrm{n}} \approx n \times 3.1$ GHz, $n \in \mathbb{N}$.

reduced susceptibility to external magnetic fields, although they lack the tunability features of SQUID-based devices.

3. Device characterisation

The experiments discussed in this section were all performed on the same device, as detailed in the preceding section.

3.1. DC and RF transmission

We first measured the current-voltage (IV) curve of the SWPA at $T = 4$ K using a four-point measurement with a current source and a voltmeter, as described in Setup-A, shown in figure 3(a). This setup enables the measurement of both the DC and RF responses of the Device Under Test (DUT) using two bias-tees. A four-way splitter and a cryogenic switch facilitate probing multiple devices, including a through SMA connector ('blank') used for calibration purposes. The result, plotted in figure 3(b), shows the characteristic nonlinear function of a Josephson junction[4]. Since the device is formed with 500 junctions in series, the gap voltage (V_{gap}) appears at 500× the $V_{\mathrm{gap,1JJ}}$ of a single junction as expected, i.e., $V_{\mathrm{gap}} = 500 \times V_{\mathrm{gap,1JJ}} \approx 1.42$ V. Therefore, from the IV curve we estimated the average $V_{\mathrm{gap,1JJ}}$ to be approximately 2.84 mV, which is conventional for Nb junctions. Similarly, from this measurement, we can extract the normal resistance R_{n} of the device, and therefore the average $R_{\mathrm{n,1JJ}}$ of the individual junctions in the array. The R_{n} and I_{c} of a junction are related by the Ambegaokar-Baratoff formula for tunnel junctions [25] via:

$$I_{\mathrm{c}} R_{\mathrm{n}} = \left(\frac{\pi \Delta}{2e}\right) \tanh\left(\frac{\Delta}{2k_{\mathrm{B}} T}\right), \tag{1}$$

where Δ is the superconducting gap energy, k_{B} is the Boltzmann constant, e is the electron charge and T is the physical temperature of the junction. Since $\Delta = eV_{\mathrm{gap}}/2$, we can rewrite the above equation as:

$$I_{\mathrm{c}} R_{\mathrm{n}} = \left(\frac{\pi V_{\mathrm{gap}}}{4}\right) \tanh\left(\frac{eV_{\mathrm{gap}}}{4k_{\mathrm{B}} T}\right). \tag{2}$$

Replacing the measured $V_{\mathrm{gap,1JJ}} = 2.84$ mV and $R_{\mathrm{n,1JJ}} = 269.2\ \Omega$ (as shown in figure 3(a)) into this equation, we calculate an $I_{\mathrm{c}} = 8.67 \pm 0.58$ μA. From the measured critical current density $J_{\mathrm{c}} = 2.5$ kA/cm^2 of the niobium trilayer deposited on the wafer and the junction's design area $A_{\mathrm{jj}} = 0.5$ μm^2 in our device, we expected

---

[4] The absence of a clear supercurrent branch in the IV curve of the measured device could be potentially attributed to the collective behaviour of outlier junctions and thermal effects in the system. A detailed exploration of this effect is out of the scope of this work.

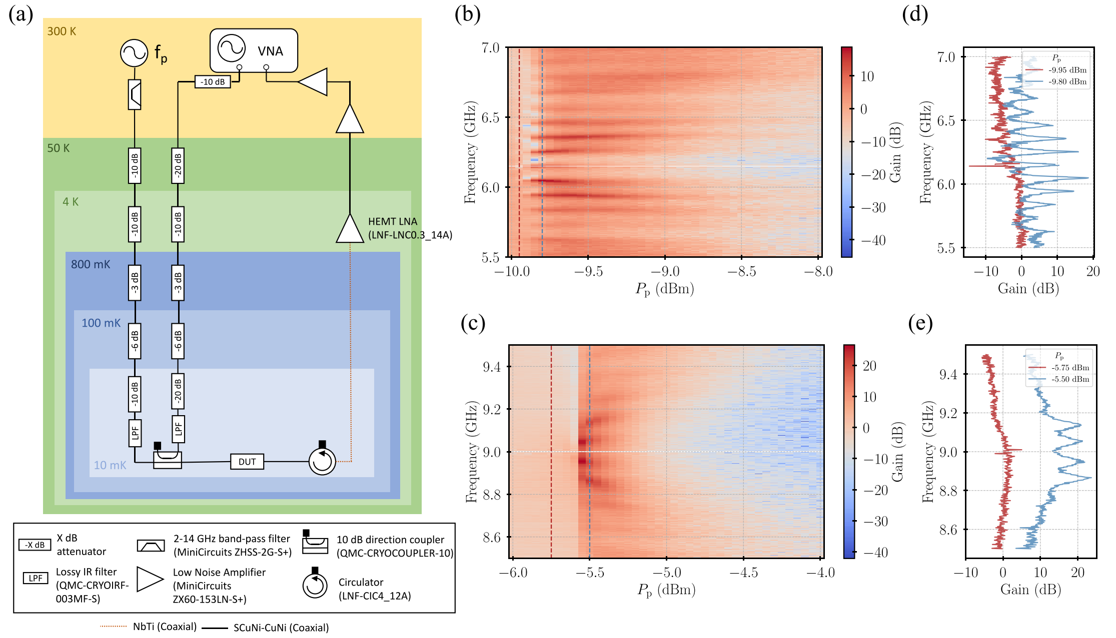

Figure 4. (a) Experimental Setup-B. (b) and (c) show 2D colormaps of the measured gain as a function of pump power (P_p) for pump frequencies $f_p = 6.15$ GHz and $f_p = 9.00$ GHz, respectively. The gain profiles corresponding to the vertical dashed lines (i.e., fixed P_p values) in (b) and (c) are plotted in (d) and (e), respectively. The data point at f_p is removed from the plots.

$I_c = 12.5$ μA. Assuming a homogeneous J_c across the wafer, the measured lower value of I_c could originate from a 36 % reduction on the area of the junctions. This effect has been observed in other devices fabricated using the same recipe and could be linked to the extra oxidation on side-wall of the junctions, which systematically reduces the junction area relative to the patterned dimensions [26].

Using the same experimental setup, we measured the RF transmission of the SWPA, and the result is plotted in figure 3(b). We notice that the S_{21} transmission periodically oscillates in frequency between $S_{21,\max} = 0$ dB and $S_{21,\min} \approx -5.42$ dB. This frequency transmission profile is a characteristic of a Fabry-Pérot cavity. In this case, the transmission peaks at approximately 3.1, 6.2 and 9.3 GHz correspond to the different resonant modes of the cavity, where $l = n\lambda/2,\ n \in \mathbb{N}$, in which l is the length of the array cavity and λ is the wavelength of the signal in the cavity. The $S_{21,\max}$ values for each mode, consistently reaching ≈0 dB, illustrates the negligible losses in the device resulting from the CPW geometry. Using the previously measured I_c value and assuming a 36 % reduction in the junction size, we calculated $L_j(I = 0) \approx 38$ pH and $C_j = 26$ fF. To estimate the remaining circuit parameters of the unit cell such as CPW's geometric inductance (L_{geo}) and shunt capacitance (C_s), we numerically fit the measured S_{21} data with the calculated S_{21} of the SWPA unit cell `ABCD` matrix cascaded by 500 times; resulting in a best fit of $L_{geo} = 11.5$ pH and $C_s = 2$ fF (red dashed line in figure 3(b)). This in turn implies a characteristic impedance of the cavity of $Z_0 = 195\ \Omega$.

3.2. Phase-preserving parametric gain

In this section, the gain is defined as the value of the transmission with the pump on, calibrated with the transmission without the pump. We used Setup-B, illustrated in figure 4(a), which incorporates 39 dB and 60 dB of attenuation in the input lines inside the cryostat to suppress thermal noise that could degrade the device's gain performance. Signal and pump are injected into the devices through the same port, and the measurements were conducted at 10 mK. Signal gain was only observed when pumping around the resonant modes of the Fabry-Pérot cavity. A 2D colormap of the measured gain when pumping at $f_p = 6.15$ GHz, i.e., around the second resonant mode, and $f_p = 9.00$ GHz, i.e., around the third resonant mode, as a function of the pump power (P_p) at the output of the signal generator is shown in figures 4(b) & (c) respectively[5]. These f_p values yielded the highest signal gain across the measurement bandwidth. The cross-sections of the 2D colormap, corresponding to two different P_p values, are shown in figures 4(d) & (e) for $f_p = 6.15$ GHz and $f_p = 9.00$ GHz respectively. We measured signal gain > 15 dB over ~350 MHz (figure 4(e)) with rapid changes of the gain with pump power P_p (an increase of 0.05 dBm would lead to > 5 dB gain increase at certain signal frequencies). This

---

[5] The first resonant mode at 3.1 GHz lies outside the bandwidth of the isolator used in the measurements. Additionally, the applied f_p values are lower than the bare resonant modes of the device due to the increase in the cavity's electrical length when the pump is applied.

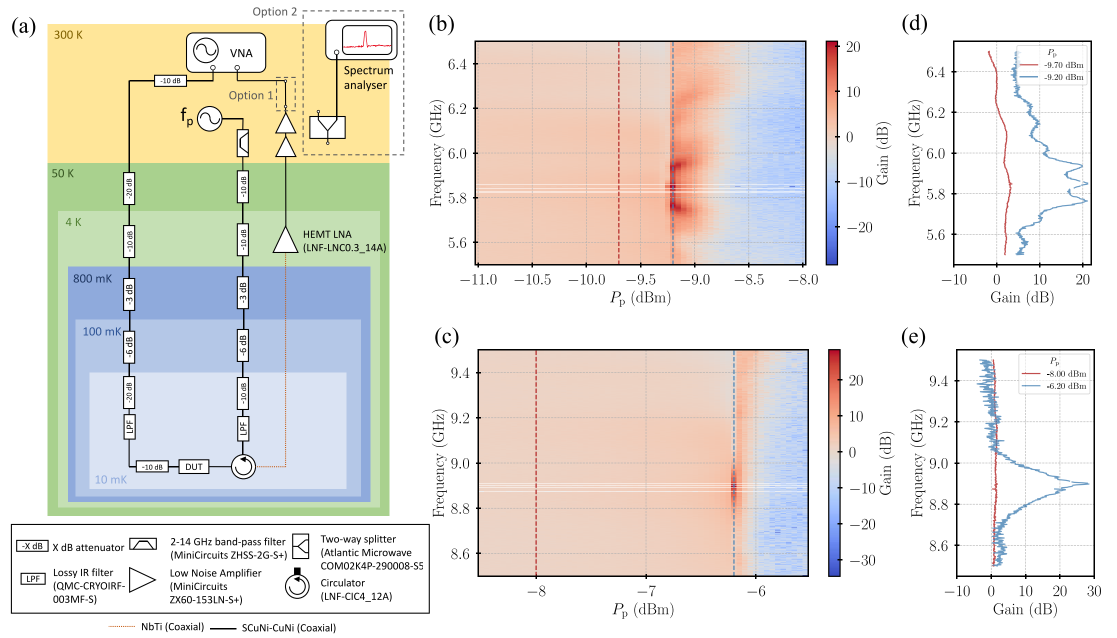

Figure 5. (a) Experimental Setup-C. Option 1(2) in the readout chain results in Setup-C1(2). (b) and (c) show 2D colormaps of the measured gain as a function of pump power (P_p) for pump frequencies $f_p = 5.85$ GHz and $f_p = 8.9$ GHz, respectively. The gain profiles corresponding to the vertical dashed lines (i.e., fixed P_p) values in (b) and (c) are plotted in (d) and (e), respectively. The data point at f_p and other data acquisition artifacts are removed from the plots.

gain sensitivity to pump power is comparable with conventional JPAs when operated for high gain [27]. Beyond the point of maximum gain, the gain decreases with increasing pump power, as expected due to effects such as pump depletion and the generation of harmonics and intermodulation products. Further increasing P_p leads to a drop in transmission, likely caused by the junctions approaching their critical current. The gain profile displays ripples with a frequency separation of $\Delta f \sim 103$MHz and 84 MHz for $f_p = 6.15$ GHz and 9.00 GHz respectively, which we suspect may originate from reflections in the experimental setup external to the device (e.g., caused by impedance mismatches), or coupling between the SWPA mode and other cavity modes.

Since the SWPA exploits the standing-wave mode of a Fabry-Pérot cavity to enhance the gain, it should in principle operate independently of the port used to inject the pump. Using Setup-C1 illustrated in figure 5(a), we investigated the different gain profiles when injecting the signal and the pump separately from the input and output ports of the device respectively. Similarly to Setup-B, we observe rapid signal gain changes with pump power as illustrated in figures 5(b) & (c) when pumping around the second and third resonant mode of the Fabry-Pérot cavity. Large values of gain were achieved as plotted in figures 5(d) & (e), corresponding to the cross-section of the 2D colormaps. Our choice of f_p in these plots corresponds to the pump frequencies that yielded the largest observed gain profiles. The overall differences in gain shape compared to the results from Setup-B may primarily arise from the difference in f_p, as even small variations in the experimental setup can lead to improved coupling efficiency at certain pump frequencies. Given the strong sensitivity of the device to pump frequency and power, such variations can significantly alter the gain response. Furthermore, we consistently observe higher gain around the second resonant mode of the array when using Setup-C1 compared to Setup-B. This behaviour may suggest a weak asymmetry in the junction array, potentially resulting from fabrication imperfections or non-ideal junction parameters.

3.3. Gain saturation

Using Setup-C1, we measured the compression point $P_{1\mathrm{dB}}$ of the SWPA. Figure 6 shows the magnitude of the signal gain when the device was pumped at $f_p = 5.85$ GHz and $P_p = 9.17$ dBm (at the output of the signal generator), as a function of the signal power P_s measured at the input of the device[6]. We calibrated the power at the input of the device using the measured losses of the input line at room temperature. The different curves represent different signal frequencies, resulting in various $P_{1\mathrm{dB}}$ values for different peak gain values. We obtained $P_{1\mathrm{dB}} = -106.2,\ -103.6,\ -101.1$ and -99.5 dBm for peak gains at 20.2, 18.2, 16.0 and 14.2 dB respectively. Since the losses of the input line decrease at cryogenic temperatures, we expect that our calculation probably underestimates the actual $P_{1\mathrm{dB}}$ of the device by 1 or 2 dB. Nevertheless, this device exhibits improved

---

[6] This configuration is almost identical to the one used for the gain profile plotted in figure 5(d) in blue.

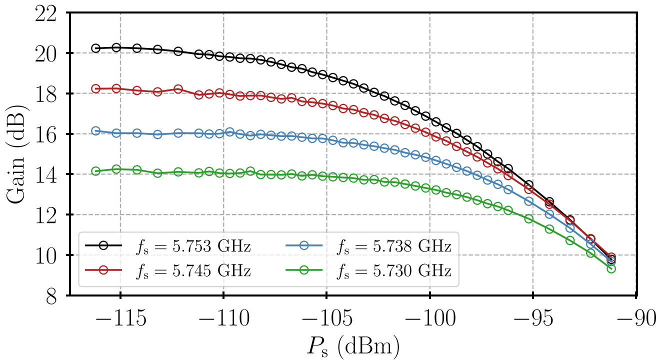

Figure 6. Measured signal gain as a function of P_s at the input of the device for different f_s values. The measurements were taken with $f_p = 5.85$ GHz and $P_p = -9.17$ dBm (at the output of the signal generator). Lines connecting the data points were added to guide the eye.

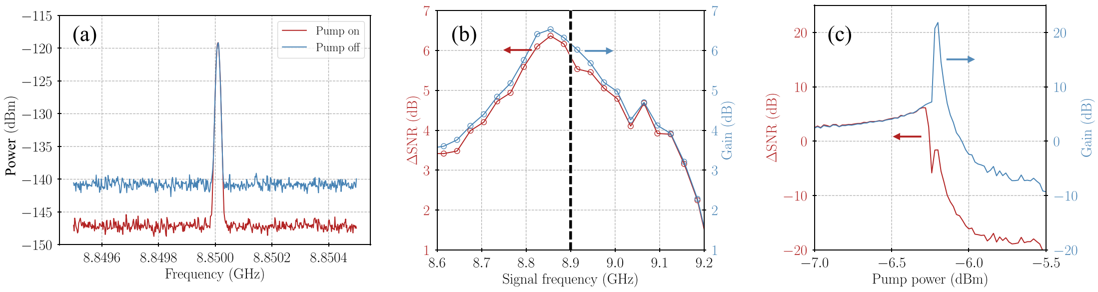

Figure 7. SNR analysis of the SWPA. All the data was taken with $f_p = 8.85$ GHz and a signal power $P_{\mathrm{V\,NA}} = -20$ dBm at the output of the VNA. (a) Measured signal power referred to the input of the SWPA for $P_p = -6.3$ dBm (at the output of the signal generator), with the pump either switched on (red) or off (blue). The data was taken within a 1 MHz window around $f_s = 8.85$ GHz. (b) ΔSNR (red) and gain (blue) as a function of f_s. The dotted vertical line indicates the pump frequency f_p used in this experiment. (c) ΔSNR (red) and gain (blue) as a function of P_p for $f_s = 8.85$ GHz.

gain saturation performance compared to conventional JPAs composed of a small number of junctions [21, 28]. While previous works have demonstrated that using larger arrays of junctions can enhance the $P_{1\mathrm{dB}}$ [19], typical values reported for devices operating at 20 dB gain lie between −120 dBm and −110 dBm. Our device shows performance beyond this range, despite its relatively simple implementation.

3.4. Signal-to-noise ratio (SNR) improvement

While a precise characterisation of an SPA noise performance requires a sophisticated measurement setup, Setup-C2 (figure 5(a)) can be used to obtain a quantitative estimation through the system's signal-to-noise ratio (SNR). This technique has been widely used to demonstrate improved noise performance in experimental readout chains when utilising an SPA [3, 27]. We measure the system's SNR with and without the pump applied to the SPA. The SNR improves only if the noise added by the SPA is less than the noise added by the following high-electron-mobility transistor (HEMT) amplifier in the readout chain. Although the SNR improvement is proportional to the gain and added noise of the SPA, a precise calibration of the system losses is needed to make the conversion. Throughout this text, we define the SNR improvement as $\Delta\mathrm{SNR} = \mathrm{SNR}_{\mathrm{pump\ on}}/\mathrm{SNR}_{\mathrm{pump\ off}}$[7].

Figure 7(a) presents the measured power around f_s, obtained using a spectrum analyser, with the pump switched on and off. The power values are referenced to the input of the SWPA. The signal tone ($f_s = 8.85$GHz) is generated using the continuous-wave mode of the Vector Network Analyser (VNA)—hence effectively functioning as a single-tone signal generator—while the pump tone at $f_p = 8.90$ GHz is provided by a separate signal generator. This operating condition matches that shown in figure 5(c). From figure 7(a), we observe a considerable reduction in the noise floor when the pump is activated, leading to an SNR improvement of approximately 6.2 dB.

This experiment was repeated for different values of f_s, as shown in figure 7(b). We find that the gain and ΔSNR are closely correlated, with the SNR improvement consistently slightly lower than the gain. This

---

[7] In linear units.

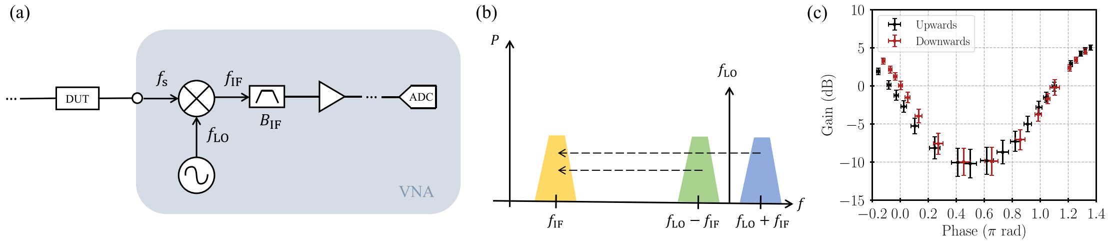

Figure 8. (a) Simplified circuit diagram of the coherent measurement scheme operated by the VNA. (b) Illustration of the frequency conversion process in a double-sideband mixer, as used in the VNA. (c) Measured signal gain plotted as a function of the measured S_{21} phase (Δ_ϕ) while varying the input signal phase using a phase shifter upward (black) and downwards (red).

behaviour is expected: for a phase-preserving amplifier, quantum mechanics requires the addition of at least half a photon of noise per mode. As a result, the signal-to-noise ratio cannot improve by more than the amplifier's gain [8]. Finally, by fixing $f_s = 8.85$GHz and $f_p = 8.90$ GHz, we examined the relationship between ΔSNR and gain as a function of pump power. The results, plotted in figure 7(c), indicate an almost one-to-one correspondence between ΔSNR and gain for pump powers below $P_p = -6.3$ dBm. However, beyond this threshold, the gain exhibits an exponential increase, exceeding 20 dB, while ΔSNR unexpectedly drops below 0 dB precisely at this transition point. This behaviour is unexpected, as it deviates from the typical performance of SPAs, where an increase in gain usually leads to improved noise performance. In conventional SPAs, higher gain suppresses the contribution of downstream amplifier noise, allowing the near-quantum-limited noise of the SPA to dominate, and thereby resulting in a substantial enhancement of the system's SNR. This abrupt divergence between gain and SNR improvement has been observed in multiple variations of SWPAs tested and appears to occur at different gain levels. This behaviour suggests the onset of excess noise or gain instability in this regime, which warrants further investigation. Nevertheless, the observed SNR improvement at moderate gain values reinforces the potential of SWPAs to enhance measurement sensitivity in certain microwave applications.

4. Phase-sensitive amplification

In this section, we describe our efforts to utilise the coherent detection mechanism of the VNA for phase-sensitive measurements of parametric amplifying devices, without requiring additional IQ mixers or a more complex experimental setup. A commercial VNA typically employs coherent detection to accurately measure the S-parameters of the DUT. As illustrated in figure 8(a), the input signal at f_s is mixed with an internal local oscillator (LO) at f_{LO} to generate an intermediate frequency (IF) signal at f_{IF}. These mixers are usually double-sideband mixers, meaning that both the $f_{LO} + f_{IF}$ and $f_{LO} - f_{IF}$ components are down-converted to the same IF frequency, as shown in figure 8(b). The IF signals are then filtered using a band-pass filter, with a user-adjustable filter bandwidth (B_{IF}). The filtered signal is subsequently amplified and processed electronically before being digitised by an analog-to-digital converter (ADC) inside the VNA. The VNA used in our experiments operates with a fixed IF frequency of $f_{IF} = 10$ MHz, while the LO frequency is adjusted accordingly to maintain a constant f_{IF} as f_s varies.

In this phase-sensitive measurement experiment (Setup-C1), we configure the VNA in continuous wave (CW) mode to generate a single signal tone at a fixed frequency f_s, which is then injected into the SWPA. The pump tone at f_p is generated by a separate signal generator, synchronised with the VNA via a shared 10 MHz reference signal to ensure phase coherence between the signal and pump tones, despite being produced by separate instruments.

Under this setup, if $f_p = f_{LO}$, the down-converted tone appears at $f_{IF} = f_{LO} \pm f_s$. Consequently, both the signal and idler generated by the SWPA are mapped onto the same IF frequency, i.e., $f_{IF} = f_p - f_s$ and $f_{IF} = f_i - f_p$, assuming $f_s < f_p$[8]. This results in phase-sensitive (or degenerate) operation. This homodyne detection scheme is similar to those used in previous experiments on microwave squeezed-state generation with JPAs [29, 30]. However, unlike in those studies, our ability to vary the signal-pump frequency offset is constrained by the fixed f_{LO} of our VNA.

With this degenerate signal-idler setup, we can measure the phase-sensitive gain performance of the SWPA. For this investigation, we set $f_p = 8.90$ GHz (as in figure 5(e)) and $f_s = 8.91$ GHz. A room-temperature variable phase shifter was introduced in the signal injection path between the output port of the VNA and the SWPA.

---

[8] Our SWPA operates in a 4WM mode.

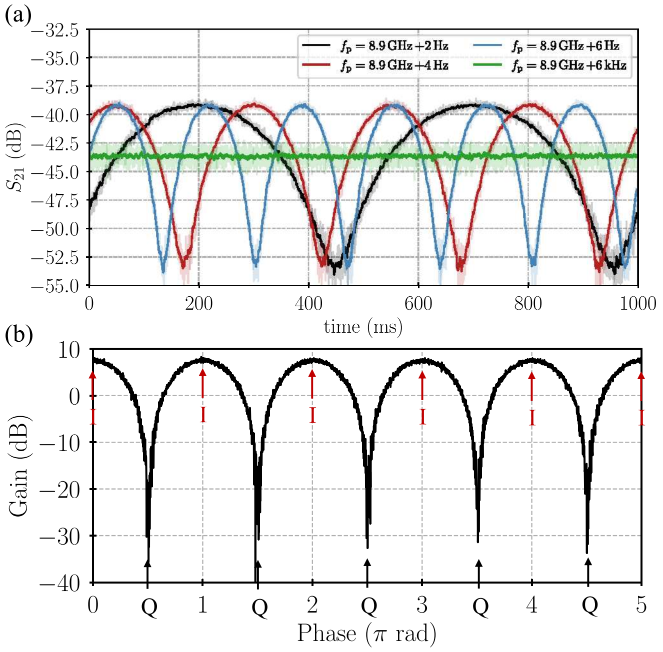

Figure 9. (a) S_{21} oscillations for different $f_p = f_{p,0} + \Delta f$, where $f_{p,0} = 8.9$ GHz. S_{21} oscillates at Δf for values below $B_{IF} = 5$ kHz, $P_p = -8$ dBm and $P_{vna} = -20$ dBm. (b) Gain as a function of the measured S_{21} phase for $f_p = 8.9$ GHz+ 6 Hz with $P_p = -8$ dBm, and $f_s = 8.91$ GHz with $P_{vna} = -20$ dBm. The local maxima and minima correspond to the amplified (*I*) and de-amplified (*Q*) quadrature respectively.

This effectively creates a phase difference Δ_ϕ between the signal and pump tones, since both sources are synchronised to the same 10 MHz reference signal. Figure 8(c) presents the measured signal gain as a function of the measured S_{21} phase, while Δ_ϕ is manually adjusted via the phase shifter—first from its minimum to maximum range (upward sweep), and then in the reverse direction (downward sweep). As expected for a phase-sensitive amplifier, the gain varies with the signal phase. At this particular pump biasing point, we achieve approximately −10 dB of de-amplification near $\Delta_\phi = 0.5\pi$ rad, with a gain peak of around 6 dB near $\Delta_\phi = 1.4\pi$ rad [9].

Next, we explored the phase-sensitive amplification when the pump frequency is shifted by Δf, i.e., $f_p = f_{p,0} + \Delta f$, where $f_{p,0} = 8.9$ GHz. This frequency shift results in a time-dependent phase shift in the pump tone, given by $\phi(t) = \Delta f \cdot t$. Therefore, we expect to observe a time-dependent variation in the measured signal transmission through the device.

Figure 9(a) presents the measured S_{21} amplitude at $f_s = 8.91$ GHz for different values of Δf. As expected, the transmission exhibits periodic oscillations over time, with the oscillation period determined by Δf. When Δf exceeds the IF bandwidth (B_{IF}) set by the user—such as in the green curve of figure 9(a), where $\Delta f = 6$ kHz rather than a few Hz—the oscillations occur too rapidly for the VNA to resolve. Instead, the VNA records only the average transmission value. This limitation is common in standard VNA S_{21} measurements, which is why phase-sensitive amplification effects are not typically observed in conventional experimental setups.

The gain oscillations in figure 9(a) correspond to the alternating acquisition of the in-phase (*I*) and quadrature-phase (*Q*) quadratures of the signal. This becomes clearer in figure 9(b), where the SWPA gain is plotted as a function of the measured signal phase for $f_p = 8.9$ GHz+ 6 Hz and $f_s = 8.91$ GHz. We observe that the maximum and minimum gain values—corresponding to the *I* and *Q* quadrature respectively—alternate every $\pi/2$ rad, since by definition *I* and *Q* have a $\pi/2$ rad phase difference. Therefore, calculating the average value of the maximas and minimas on the plot, we extract the amplification (*I* quadrature) and the de-amplification (*Q* quadrature) gain for this particular signal frequency and power configuration. As can be seen, our simple parametric device consistently achieves more than −30 dB of de-amplification, suggesting that it could potentially be used to squeeze the vacuum noise.

Finally, we investigated the phase-sensitive amplification of the SWPA as a function of pump power. Figure 10 presents the gain magnitude for both the *I* and *Q* quadratures as the pump power is swept from −20 dBm to approximately −6 dBm, where the junctions reach their critical current I_c. We observe an

---

[9] The apparent 'bifurcation' in figure 8(c) for $\Delta_\phi < 0.4\pi$ rad is likely caused by reduced accuracy of the mechanical phase shifter near its minimum range, combined with phase instability due to the use of non-phase-stable coaxial cables in the setup. This instability could have lead to phase shift between the pump and signal paths over the time of taking the measurements.

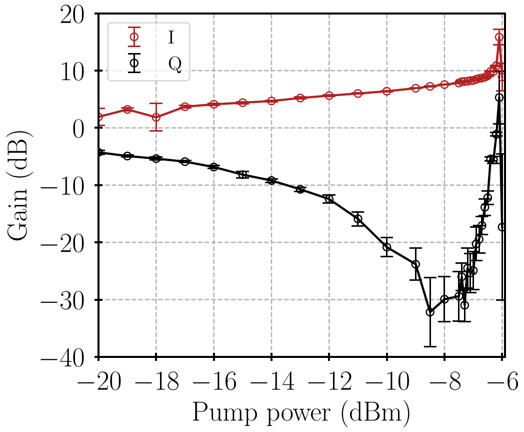

Figure 10. Measured amplification (red)—*I* quadrature—and de-amplification (black)—*Q* quadrature—gain as a function of the pump power level in the signal generator ($P_{\mathrm{vna}} = -13$ dBm). We fix $f_p = 8.9$ GHz+ 6 Hz and $f_s = 8.91$ GHz.

asymmetry between the two quadratures: the de-amplification increases more rapidly with pump power than the amplification. Additionally, the de-amplification deteriorates sharply for pump powers approaching the critical current of the junctions. The origin of this asymmetry is not yet fully understood and remains an active area of investigation. Nevertheless, we measured a phase-sensitive extinction ratio (PSER), defined as the difference between the maximum phase-sensitive amplification and de-amplification, reaching values as high as 42.30 ± 2.81 dB. This value is comparable to the highest PSER reported in JPAs [31, 32], further highlighting the potential of the SWPA to function as an effective squeezer for suitable applications.

5. Conclusion

In this paper, we have described the phase-preserving and phase-sensitive parametric amplification of a standing-wave parametric device comprising an array of 500 Josephson junctions. The device operates similarly to a conventional JPA but with a significantly lower *Q*-factor, where a Fabry-Pérot cavity is formed by impedance mismatches between the embedded junctions and the 50 Ω sections. From DC and RF transmission measurements, we extracted the device's circuit parameters, revealing a possible 36% deviation in junction size from the target value, likely due to sidewall oxidation of the junctions. Nevertheless, we observed the expected standing-wave RF transmission profile characteristic of a Fabry-Pérot resonator. When pumped near the resonant modes of the array, the device exhibited 4WM gain exceeding 15 dB over a bandwidth of approximately 350 MHz, with peak gains reaching 30 dB at specific frequency points. We measured a 1 dB compression point of $P_{1\mathrm{dB}} = -106.2$ dBm at $G \sim 20$ dB, demonstrating an improvement over most conventional JPAs. Additionally, the device achieved an SNR enhancement of up to 6.2 dB compared to the HEMT amplifier used in our measurement setup, albeit at a lower gain value. Finally, we measured a phase-sensitive extinction ratio of 42.30 ± 2.81 dB, highlighting the potential of the device for noise squeezing applications.

Acknowledgments

This research is supported by the European Commission's Horizon Europe Horizon-Infra-2022-Tech-01 programme RADIOBLOCKS (Project ID: 101093934), the European Research Council (ERC) under the European Union's Horizon 2020 research and innovation programme with grant agreement No. [803862] (Project [SPA4AstroQIT]), the UKRI Quantum Technology for Fundamental Physics programme under the project Quantum Sensor for Hidden Sector (QSHS, ST/T006277/1) and STFC Capital Fund (ST/X004880/1). J. Navarro Montilla's D.Phil. studentship is supported by the STFC and the Foley-Bejar Scholarship from the Balliol College, Oxford. For the purpose of Open Access, the author has applied a CC BY public copyright licence to any Author Accepted Manuscript (AAM) version arising from this submission.

Data availability statement

All data that support the findings of this study are included within the article (and any supplementary files).

References

[1] Smith D M P, Bakker L, Witvers R H, Woestenburg B E M and Palmer K D 2013 Low noise amplifier for radio astronomy *Int. J. Microwave Wireless Technolog.* **5** 453461

[2] Bockstiegel C, Gao J, Vissers M R, Sandberg M, Chaudhuri S, Sanders A, Vale L R, Irwin K D and Pappas D P 2014 Development of a broadband nbtin traveling wave parametric amplifier for mkid readout *J. Low Temp. Phys.* **176** 476–82

[3] Macklin C, O'Brien K, Hover D, Schwartz M E, Bolkhovsky V, Zhang X, Oliver W D and Siddiqi I 2015 A near–quantum-limited josephson traveling-wave parametric amplifier *Science* **350** 307–10

[4] Backes K M *et al* 2021 A quantum enhanced search for dark matter axions *Nature* **590** 238–42

[5] Ramanathan K, Klimovich N, Basu Thakur R, Eom B H, Leduc H G, Shu S, Beyer A D and Day P K 2023 Wideband direct detection constraints on hidden photon dark matter with the qualiphide experiment *Phys. Rev. Lett.* **130** 231001

[6] Fraudet D *et al* 2025 Direct detection of down-converted photons spontaneously produced at a single josephson junction *Phys. Rev. Lett.* **134** 013804

[7] Bienfait A *et al* 2016 Reaching the quantum limit of sensitivity in electron spin resonance *Nat. Nanotechnol.* **11** 253–7

[8] Caves C M 1982 Quantum limits on noise in linear amplifiers *Phys. Rev. D* **26** 1817–39

[9] Castellanos-Beltran M A and Lehnert K W 2007 Widely tunable parametric amplifier based on a superconducting quantum interference device array resonator *Appl. Phys. Lett.* **91** 08350908

[10] Kissling C, Gaydamachenko V, Kaap F, Khabipov M, Dolata R, Zorin A B and Grünhaupt L 2023 Vulnerability to parameter spread in josephson traveling-wave parametric amplifiers *IEEE Trans. Appl. Supercond.* **33** 1–6

[11] Peatáin SÓ, Dixon T, Meeson P J, Williams J M, Kafanov S and Pashkin Y A 2023 Simulating the effects of fabrication tolerance on the performance of josephson travelling wave parametric amplifiers *Superconductor Science and Technology* **36** 045017

[12] Elkin S T, Haider M and Roth T E 2024 Multiphysics numerical method for modeling josephson traveling-wave parametric amplifiers *IEEE Journal on Multiscale and Multiphysics Computational Techniques* **9** 247–57

[13] Montilla J N, Driessen E F C, Barbier A, Boussaha F, Chaumont C and Tan B-K 2022 Exploring the limits of the tunnel junction fabrication technique for josephson junctions twpa and the preliminary characterisation results *32nd IEEE International Symposium on Space THz Technology (Baeza, Spain, 16–20 October 2022)*

[14] Montilla J N, Klimovich N, Arnaud B, Driessen E F C and Tan B-K 2024 *Investigating Pin-Holes Issues in Josephson Junction Travelling Wave Parametric Amplifiers Requiring Large Area of Dielectric Layer 33rd IEEE International Symposium on Space THz Technology (Charlottesville, Virginia, USA, 7–11 April 2024)*

[15] Le Gal G, Butseraen G, Ranadive A, Cappelli G, Fazliji B, Bonet E, Eyraud E, Planat L and Roch N 2025 Gain compression in josephson traveling-wave parametric amplifiers *Physical Review Applied* **24** 014022

[16] Grebel J, Bienfait A, Dumur É., Chang H-S, Chou M H, Conner C R, Peairs G A, Povey R G, Zhong Y P and Cleland A N 2021 Flux-pumped impedance-engineered broadband Josephson parametric amplifier *Appl. Phys. Lett.* **118** 142601

[17] Roy A and Devoret M aug 2016 Introduction to parametric amplification of quantum signals with josephson circuits *C.R. Phys.* **17** 740–55

[18] Zhou X, Schmitt V, Bertet P, Vion D, Wustmann W, Shumeiko V and Esteve D 2014 High-gain weakly nonlinear flux-modulated josephson parametric amplifier using a squid array *Phys. Rev. B* **89** 214517

[19] Planat L, Dassonneville Rémy, Martínez J P, Foroughi F, Buisson O, Hasch-Guichard W, Naud Cécile, Vijay R, Murch K and Roch N 2019 Understanding the saturation power of josephson parametric amplifiers made from squid arrays *Phys. Rev. Appl.* **11** 034014

[20] Yamamoto T, Inomata K, Watanabe M, Matsuba K, Miyazaki T, Oliver W D, Nakamura Y and Tsai J S 2008 Flux-driven josephson parametric amplifier *Appl. Phys. Lett.* **93** 042510

[21] Eichler C, Salathe Y, Mlynek J, Schmidt S and Wallraff A 2014 Quantum-limited amplification and entanglement in coupled nonlinear resonators *Phys. Rev. Lett.* **113** 110502

[22] Castellanos-Beltran M A, Irwin K D, Hilton G C, Vale L R and Lehnert K W 2008 Amplification and squeezing of quantum noise with a tunable josephson metamaterial *Nat. Phys.* **4** 929–31

[23] Frasca S, Roy C, Beaulieu G and Scarlino P 2024 Three-wave-mixing quantum-limited kinetic inductance parametric amplifier operating at 6 t near 1 k *Phys. Rev. Appl.* **21** 024011

[24] Sivak V V, Shankar S, Liu G, Aumentado J and Devoret M H 2020 Josephson array-mode parametric amplifier *Phys. Rev. Appl.* **13** 024014

[25] Tinkham M 2004 *Introduction to Superconductivity* (Courier Corporation)

[26] Navarro Montilla J 2024 *Development of Josephson Travelling Wave Parametric Amplifiers PhD thesis, University of Oxford* Submitted in October 2024. Yet to be published

[27] Planat L 2020 *Resonant and Traveling-Wave Parametric Amplification Near the Quantum Limit. PhD thesis, University of Grenoble Alpes*

[28] Mahboob I, Toida H, Kakuyanagi K, Nakamura Y and Saito S 2022 A three-dimensional josephson parametric amplifier *Applied Physics Express* **15** 062005

[29] Yurke B, Kaminsky P G, Miller R E, Whittaker E A, Smith A D, Silver A H and Simon R W 1988 Observation of 4.2-k equilibrium-noise squeezing via a josephson-parametric amplifier *Phys. Rev. Lett.* **60** 764–7

[30] Movshovich R, Yurke B, Kaminsky P G, Smith A D, Silver A H and Simon R W 1991 Vacuum noise squeezing at microwave frequencies using a josephson parametric amplifier *IEEE Trans. Magn.* **27** 2658–60

[31] Zhong L *et al* 2013 Squeezing with a flux-driven josephson parametric amplifier *New J. Phys.* **15** 125013

[32] Bienfait A *et al* 2017 Magnetic resonance with squeezed microwaves *Phys. Rev. X* **7** 041011